

High-Entropy Sulfides as Highly Effective Catalysts for the Oxygen Evolution Reaction

Ling Lin, Ziming Ding, Guruprakash Karkera, Thomas Diemant, Mohana V. Kante, Daisy Agrawal, Horst Hahn, Jasmin Aghassi-Hagmann, Maximilian Fichtner, Ben Breitung,* and Simon Schweidler*

With respect to efficient use of diminishing or harder to reach energy resources, the catalysis of processes that will otherwise require high overpotentials is a very important application in today's world. As a newly developed class of materials, high-entropy sulfides (HESs) are promising electrocatalysts for a variety of different reactions. In this report, HESs containing five or six transition metals are synthesized in a one-step mechanochemical process. Seven HESs of *Pnma* ($M:S \approx 1:1$) and three *Pa-3* ($M:S = 1:2$) structures are investigated as electrocatalysts for the oxygen evolution reaction (OER). The performances and properties of the HESs with different compositions and structures are compared with each other and with commercial IrO_2 as reference material, in terms of OER overpotential, Tafel slope, electrochemically active surface area, ionic conductivity, and durability. The structural and chemical properties of these HESs are determined by X-ray diffraction, transmission electron microscopy, scanning electron microscopy, X-ray photoelectron spectroscopy, and energy-dispersive X-ray spectroscopy. Most of the HESs show excellent and promising performance as OER electrocatalysts under alkaline conditions, and outperform the reference OER catalyst IrO_2 .

reaction (OER) is a four-electron-transfer process,^[1–3] with unfortunately complicated mechanism and slow reaction kinetics resulting in high overpotential. These characteristics can be seen as a crucial bottleneck limiting the large-scale application of electrocatalytic water splitting. To solve the problem of large overpotentials, many (transition) metal-based materials (oxides, phosphides, sulfides) have been investigated as catalysts to reduce the overpotential and thus to increase the efficiency of the OER reaction. Transition-metal sulfides are an important candidate for OER catalysts because they exhibit highly variable redox chemistry and high activities.^[4–6]

High-entropy materials (HEMs), as a novel material class, have gained rising popularity in recent years.^[7] The high-entropy concept is based on the inclusion of many different elements into a single-phase structure, which leads to a high configurational

entropy (S_{config}). S_{config} can be calculated according to the following formula (Equation (1)), which is based on the Boltzmann and Gibbs interpretation of entropy.^[8,9]


$$S_{\text{config}} = -R \left[\left(\sum_{i=1}^N x_i \ln x_i \right)_{\text{cation-site}} + \left(\sum_{j=1}^M x_j \ln x_j \right)_{\text{anion-site}} \right] \quad (1)$$

1. Introduction

Due to global environmental and energy crises, research in sustainable energy storage and conversion has attracted wide attention. To replace fossil fuels, clean hydrogen produced by electrocatalytic water splitting is one of the most important candidates. However, the respective anodic oxygen evolution

L. Lin, Z. Ding, M. V. Kante, H. Hahn, J. Aghassi-Hagmann, M. Fichtner, B. Breitung, S. Schweidler
Institute of Nanotechnology
Karlsruhe Institute of Technology (KIT)
Hermann-von-Helmholtz-Platz 1, 76344, Germany
E-mail: ben.breitung@kit.edu; simon.schweidler@kit.edu

L. Lin, Z. Ding, D. Agrawal
Department of Materials- and Geosciences
Technical University Darmstadt
64289 Darmstadt, Germany

 The ORCID identification number(s) for the author(s) of this article can be found under <https://doi.org/10.1002/ssstr.202300012>.

© 2023 The Authors. Small Structures published by Wiley-VCH GmbH. This is an open access article under the terms of the Creative Commons Attribution License, which permits use, distribution and reproduction in any medium, provided the original work is properly cited.

DOI: 10.1002/ssstr.202300012

Z. Ding
Karlsruhe Nano Micro Facility (KNMF)
Karlsruhe Institute of Technology (KIT)
Eggenstein-Leopoldshafen, 76344, Germany

G. Karkera, T. Diemant, M. Fichtner
Electrochemical Energy Storage
Helmholtz Institute Ulm (HIU)
Helmholtzstraße 11, 89081, Germany

H. Hahn
School of Chemical, Biological and Materials Engineering
University of Oklahoma
Norman 73019, OK, USA

Herein, R is the ideal gas constant, x_i and x_j are the molar fractions of the i th component of cation and j th component of anion, while N and M represent the numbers of cation and anion components, respectively. Originating from alloy systems,^[10,11] the concept of high entropy has now developed also to various ceramic materials, such as oxides,^[12,13] nitrides,^[14] carbides,^[15,16] fluorides,^[17,18] silicides,^[19] chalcogenides,^[20–25] and many more.

HEMs show promising properties in a broad range of applications, of which catalysis is an important branch.^[26–28] The unique configuration of the elements in the structure, which is also found on the surface of the particles, makes this class of materials exciting for catalysis. The homogeneous distribution of the elements in the crystal lattice is associated with a large number of interactions between the elements, leading to tailorable catalytic properties according to the element composition and stoichiometry. These effects are called cocktail effects and increase the complexity of high-entropy compounds even further. Moreover, an occurring distortion of the lattice of HEMs, due to different ionic sizes and electronegativities of the incorporated elements, promotes activation and transport of active species.^[28]

Very recently, high-entropy sulfides (HESs) have been reported to be very promising catalysts for OER. In a first report in 2020,^[22] Cui et al. synthesized cubic $Fm\bar{3}m$ -structured $(\text{CrMnFeCoNi})_9\text{S}_8$ by a pulsed thermal decomposition method, and this HES served as a good OER catalyst. Later, in 2021,^[23] Nguyen et al. reported pyrite $Pa\bar{3}$ -structured FeNiCoCrXS_2 (with $X = \text{Mn, Cu, Zn, or Al}$) synthesized by a two-step solvothermal method. In 2022,^[25] Lei et al. prepared carbon-fiber-supported HES (CoZnCdCuMnS@CF) nanoarrays by a mild cation exchange strategy and reported their good catalytic activity and stability for overall water splitting.

In the present report, building on previous work of equimolar metal HESs of pyrite ($Pa\bar{3}$) and orthorhombic ($Pnma$) structures,^[24] we present new non-equimolar HESs with $Pnma$ structure obtained by a one-step mechanochemical synthesis reaction. All homogeneously mixed HESs have polycrystalline particles and sizes ranging from tens to hundreds of nanometers. The composition and structure of the HESs are investigated and their potential as OER catalysts is assessed.

2. Results and Discussion

As promising catalysts for the OER reaction, 3d transition-metal-based electrocatalysts, for example, NiFe-based materials, have attracted much attention due to their low cost and outstanding electrocatalytic performance.^[29,30] Improved OER performance can be achieved by doping these catalysts with other metals such as Co,^[5] Mn,^[31] or Ti,^[32] which worked for metal sulfides, oxides, and hydroxides by tuning the electronic structure of the active centers. Based on the previous research results, we incorporated the most active elements into a single-phase high-entropy structure and reported several types of HESs containing five or six different transition metals (Ti, Cr, Mn, Fe, Co, Ni, Cu, Ag, and Mo). The samples were synthesized by a simple one-step high-energy ball-milling method. All prepared HESs are listed in **Table 1**. Since all samples were obtained directly by a one-step ball-milling solid-state synthesis procedure under an inert

Table 1. Overview of the synthesized different HESs.

Composition	Structure	S_{config}	Abbreviation
$\text{TiFe}_2\text{Co}_2\text{Ni}_3\text{MoS}_{10}$	$Pnma$	1.52 R	HESMo
$\text{TiFe}_2\text{Co}_2\text{Ni}_3\text{MoMn}_2\text{S}_{12}$	$Pnma$	1.72 R	HESMoMn
$\text{TiFe}_2\text{Co}_2\text{Ni}_3\text{MoCu}_2\text{S}_{12}$	$Pnma$	1.72 R	HESMoCu
$\text{TiFe}_2\text{Co}_2\text{Ni}_3\text{MoCu}_2\text{S}_{11}$	$Pnma$	1.72 R	HESMoCu-1
$\text{TiFe}_2\text{Co}_2\text{Ni}_3\text{MoAg}_2\text{S}_{11}$	$Pnma$	1.72 R	HESMoAg-1
$\text{TiFe}_2\text{Co}_2\text{Ni}_3\text{Cu}_2\text{S}_{10}$	$Pnma$	1.56 R	HESCu
MnFeNiCoCrS_5	$Pnma$	1.61 R	HES1CoCr
MnFeNiCoCrS_{10}	$Pa\bar{3}$	1.61 R	HES2CoCr
MnFeNiCoCuS_{10}	$Pa\bar{3}$	1.61 R	HES2CoCu
MnFeNiTiCrS_{10}	$Pa\bar{3}$	1.61 R	HES2TiCr

atmosphere and without further processing, the compositions in **Table 1** were calculated based on the ratio of the starting materials. To confirm the compositions, inductively coupled plasma optical emission spectroscopy (ICP-OES) and energy-dispersive X-Ray spectroscopy (EDX) were performed for six non-equimolar HES, the results are summarized in **Table S1**, Supporting Information. The ICP-OES and EDX analyses of the other four equimolar metal HESs (HES1CoCr, HES2CoCr, HES2CoCu, and HES2TiCr) can be found in a previous report.^[24]

To evaluate the crystal structure of the HESs materials, powder X-ray diffraction (XRD) measurements and Rietveld analysis were performed. A comparison of the obtained XRD patterns is shown in **Figure 1**. Depending on the M:S ratio of 1:1 or 1:2, the HESs form orthorhombic ($Pnma$) or pyrite ($Pa\bar{3}$) phases. The six new HESs with non-equimolar metal stoichiometry, with exception of HESMoMn where a small impurity is detected, show a $Pnma$ crystal structure like the equimolar-metal HES1CoCr. The Rietveld refinement of the HESMo pattern as an example (**Figure 2**) confirms the predominant $Pnma$ phase with a unit cell

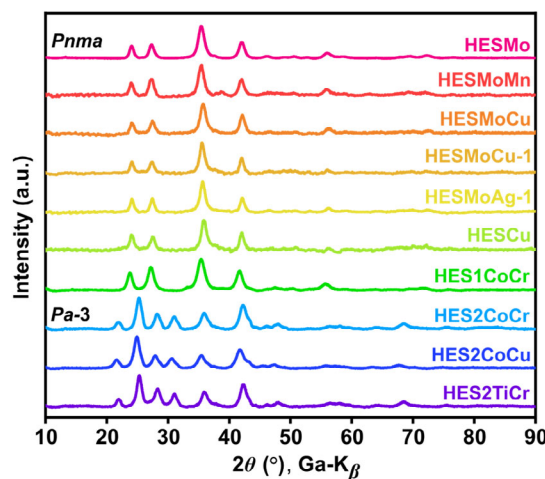


Figure 1. Comparison of X-Ray diffraction (XRD) patterns of high-entropy sulfides (HESs) with different elemental composition. The abbreviations can be found in **Table 1**.

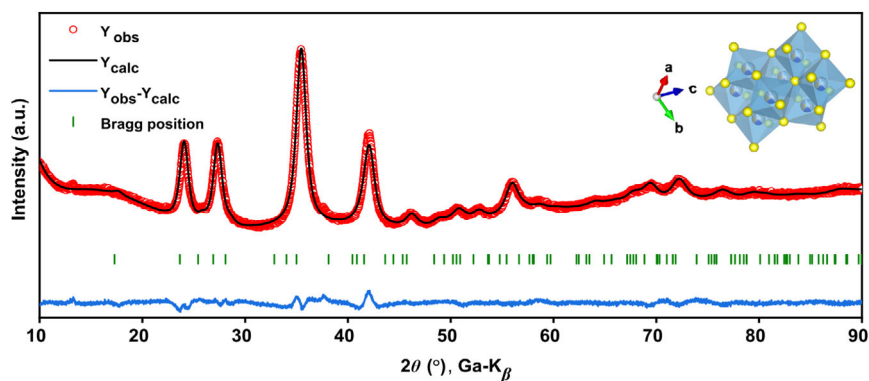


Figure 2. Example for the Rietveld refinement of HESMo.

volume of $110.2(4) \text{ \AA}^3$ and lattice parameters $a = 5.489(2) \text{ \AA}$, $b = 3.404(8) \text{ \AA}$, and $c = 5.894(1) \text{ \AA}$. The Rietveld refinement of four equimolar metal HESs (*Pnma* structured HES1CoCr, *Pa-3* structured HES2CoCr, HES2CoCu, and HES2TiCr) have been reported in previous study.^[24]

Since the morphology of catalysts can strongly influence the catalytic performance,^[33] the morphology of HESs was studied by scanning electron microscopy (SEM). The size of polycrystalline HES particles varies in a range from tens to hundreds of nanometers, as revealed by SEM micrographs in Figure S1, Supporting Information. The particles either consist of a large number of small, irregularly shaped agglomerated crystallites or smaller particles are distributed on the surface of some relatively larger blocks. Transmission electron microscopy (TEM) was performed to further investigate the structural details. As an example, **Figure 3a** shows high-resolution TEM (HR-TEM) images of HESMo. The yellow-circled area refers to the (111) diffraction plane with lattice spacing of 0.26 nm. In addition, selected area electron diffraction (SAED) measurements were performed for HESMo (Figure 3b). For HESMo, the diffraction ring indexing is in agreement with the XRD measurements, confirming the *Pnma* space group. The elemental distribution of HESMo was studied by scanning TEM (STEM)-EDX mapping

(Figure 3c). All elements are homogeneously distributed at the nanometer scale, with no indication of segregation, which allows them to act independently as catalytic active centers. Recently, Mössbauer spectroscopy was performed on similar HESs, also prepared by a ball-milling process, to evaluate the chemical environment of the incorporated Fe.^[24] The results showed that the Fe was embedded in a very similar chemical environment, indicating a homogeneous distribution of all elements in the crystal structure rather than agglomeration or segregation of certain elements that would lead to different chemical environments. In conjunction with the high-angle annular dark-field (HAADF)/EDX mapping shown in Figure S2, Supporting Information, this indicates a homogeneous distribution of elements at the atomic level and on a larger scale.

The catalytic OER performance of the HESs was tested in comparison to commercial IrO_2 in an O_2 -saturated 1 M KOH electrolyte using a typical three-electrode setup (for more details, see Experimental Section). To compare the catalytic activity of the OER reaction between HESs and IrO_2 , the polarization curves (**Figure 4a,b**) were measured by linear sweep voltammetry (LSV). The overpotentials at different current densities are summarized in **Table 2**. The reference catalyst IrO_2 (see Figure S3, Supporting Information, for morphology) requires an

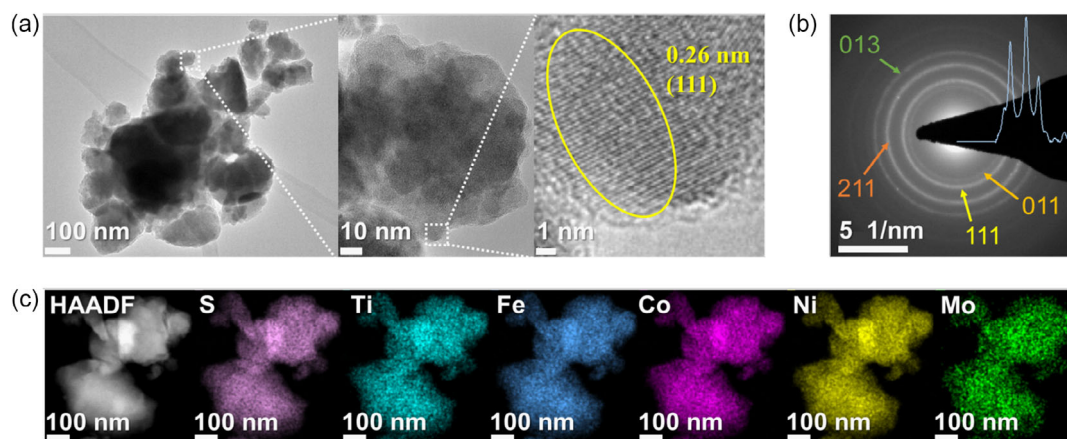


Figure 3. a) High-resolution transmission electron microscope (HR-TEM) micrographs, b) selected area electron diffraction (SAED) pattern, and c) scanning TEM energy-dispersive X-ray spectroscopy (STEM-EDX) mapping of HESMo.

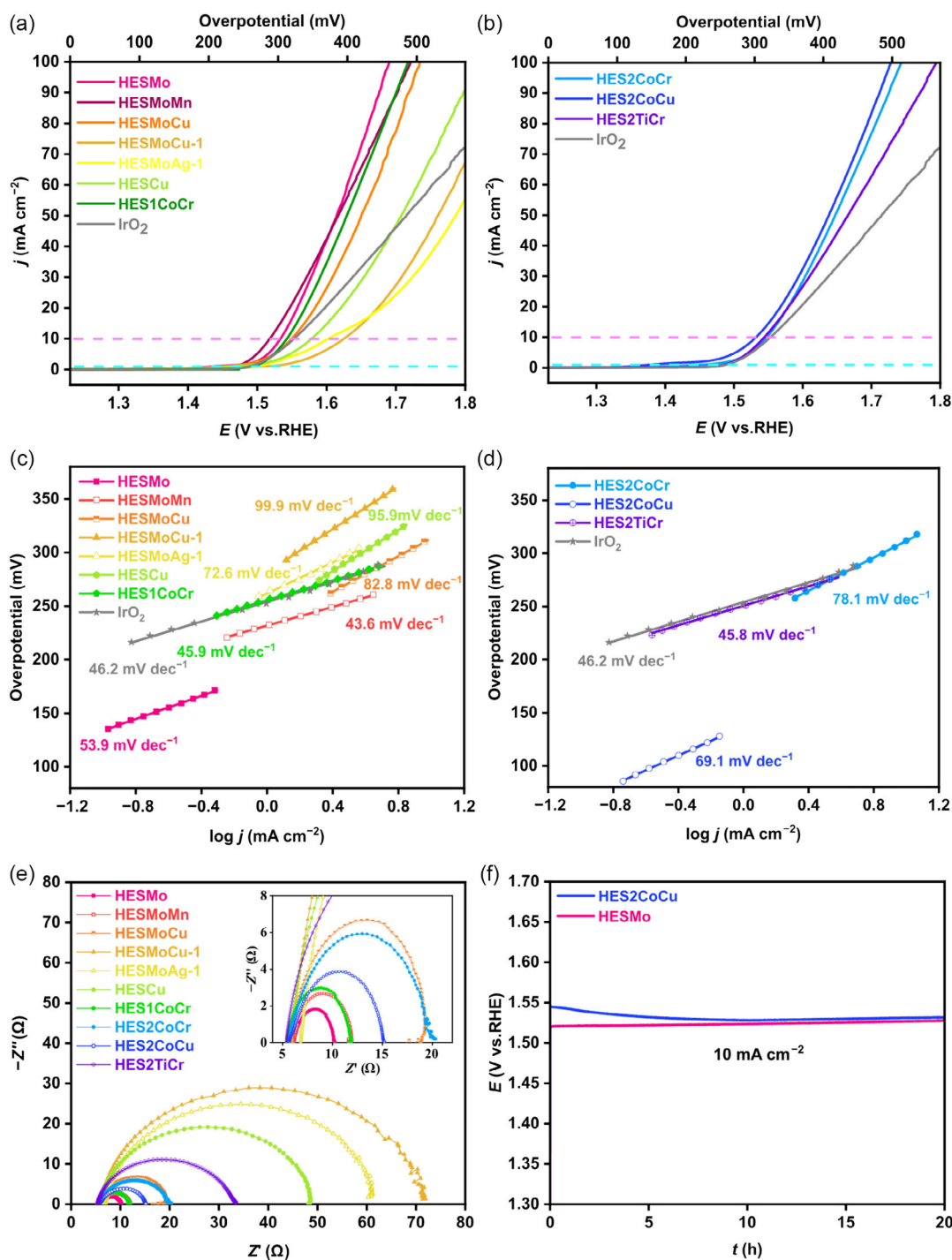


Figure 4. Oxygen evolution reaction (OER) performance. a) Polarization curves of *Pnma* structured HESs and IrO₂. b) Polarization curves of HES1CoCr, *Pa-3*-structured HES2s and IrO₂. The blue- and pink-dashed lines mark the values for overpotential at onset and 10 mA cm⁻², respectively. c, d) Tafel slopes derived from corresponding polarization curves. e) electrochemical impedance spectroscopy (EIS) spectra of all HESs in a three-electrode cell with an O₂-saturated 1 M KOH electrolyte. f) Chronopotentiometry of HESMo and HES2CoCu for 20 h at 10 mA cm⁻².

overpotential of 258 mV to reach a current density of 1 mA cm⁻² (defined as the onset overpotential) and an overpotential of 323 mV at 10 mA cm⁻², which are comparable to values reported in the literature.^[34]

Compared to IrO₂, all HESs show either better or comparable catalytic activities. Among the HESs with *Pnma* structure (Figure 4a), especially HESMo, HESMoMn, HESMoCu, and HES1CoCr exhibit better OER performance than IrO₂.

Table 2. Comparison of the OER activity of HESs and IrO₂ (red and blue values represent improved and lower performance than IrO₂, respectively).

Electrocatalyst	Overpotential [mV]				Tafel slope [mV dec ⁻¹]
	Onset @1 mA cm ⁻²	@10 mA cm ⁻²	@50 mA cm ⁻²	@100 mA cm ⁻²	
HESMo	205	303	384	460	53.9
HESMoMn	237	288	386	491	43.6
HESMoCu	225	319	420	504	82.8
HESMoCu-1	281	395	530	–	99.9
HESMoAg-1	268	372	556	–	72.6
HESCu	221	348	477	–	95.9
HES1CoCr	261	313	399	488	45.9
HES2CoCr	224	317	417	513	78.1
HES2CoCu	148	302	408	498	69.1
HES2TiCr	256	314	436	564	45.8
IrO ₂	258	323	484	–	46.2

HESMo exhibits the best overall catalytic activity for OER: the overpotentials at 1 (onset), 10, 50, and 100 mA cm⁻² are 205, 303, 384, and 460 mV, respectively. HESMoMn shows the lowest overpotential in the current density range of 1.5–45.5 mA cm⁻², the overpotentials are 237, 288, 386, and 491 mV at 1 (onset), 10, 50, and 100 mA cm⁻², respectively. The catalytic activity of HESMoMn was found to be slightly better than that of HESMo, in terms of overpotential at current density below 45.4 mA cm⁻² and Tafel slope (derived from LSV during low current density). This improvement could be attributed to the incorporation of Mn that tunes the electronic structure of active metal centers (such as Co) to effectively enhance their intrinsic activity.^[35] In another study, it was found that doping Mn into Ni-based hydroxides can improve OER activities by adjusting the adsorption energy difference between *O and *OH.^[36] Compared with HESCu, the overpotentials in HESMoCu and HESMo are greatly reduced by introduction of Mo or replacement of Cu by Mo, indicating that Mo improves the catalytic OER performance. A recent report suggests that the coordination of Mo into FeCoNi weakens OH* bonding and speeds up the rate-determining OH* deprotonation step of OER, leading to improved OER performance.^[37]

In addition, during the synthesis, when the Cu precursor is changed from CuS (Cu²⁺) to Cu₂S (Cu¹⁺), the overpotential of HESMoCu-1 increases significantly, so it can be assumed that this is also the case when HESMoCu is changed to HESMoCu-1. A comparable result was also found for copper oxides. Deng et al. reported that CuO and Cu(OH)₂ catalyze OER ~10 times more efficiently than Cu and Cu₂O, due to the fact that metastable Cu³⁺ species were detected only on CuO and Cu(OH)₂ surfaces, which could be considered as a catalytically active species for OER.^[38] Similar poor OER performance is also observed for HESMoAg-1. Therefore, it can be assumed that the incorporation of the +1 metal cations Cu or Ag leads to a significant deterioration of the OER activity, which may be due to the lack of formation of efficient catalytically active species of these metal ions.

To compare the OER reaction kinetics, Tafel slopes are derived from the polarization curves. Figure 4c shows that HESMoMn, HES1CoCr, and HESMo exhibit comparable Tafel slopes of 43.6,

45.9, and 53.9 mV dec⁻¹, respectively, close to IrO₂ with 46.2 mV dec⁻¹. The lower the Tafel slope, that is, the smaller the change in overpotential, the faster the increase in current density, and the better the electrocatalytic performance of OER.

While HES1CoCr showed slightly worse performance than HESMo and HESMoMn, it performed better than the other four HESs. Since HES1CoCr has an equimolar metal composition and the incorporated metals (Fe, Co, Ni, Mn, Cr) differ from the other six *Pnma* structured non-equimolar metal HESs, it is not suitable for a direct comparison with other *Pnma* samples to explore the elemental influence. The main intention behind HES1CoCr was to study the influence of different structures and sulfur content by comparing it with HES2CoCr.

All HES2s with *Pa-3* structure require lower overpotentials than IrO₂ (Figure 4b). The best performing catalyst, HES2CoCu, shows overpotentials of 148, 302, 408, and 498 mV at 1 (onset), 10, 50, and 100 mA cm⁻², respectively. Replacing Co with Ti results in slightly higher overpotential than for the other HES2s, possibly due to the lack of synergy between Ti and other transition metals such as Fe,^[39] while Co–Fe catalysts are known for its synergistic effect.^[40]

Furthermore, in contrast to the elemental composition of the transition metals, the metal–sulfur ratio probably also has an effect on the catalytic activity. This becomes clear in the direct comparison of HES1CoCr and HES2CoCr. Both materials have similar morphology (Figure S1, Supporting Information) and transition-metal composition with majority of 2+ oxidation states (except Fe and Cr) and differ only in the ratio of sulfur anions (S²⁻ and S₂²⁻).^[24] Therefore, it can be assumed that the higher proportion of metal cations is the main factor for the OER activity. Thus, HES1CoCr (M:S = 1:1) shows a bit better OER activity compared to HES2CoCr (M:S = 1:2), as evidenced by slightly lower overpotential above the current densities of 5 mA cm⁻² and lower Tafel slope (Table 2).

Since the OER is a surface-dependent catalytic reaction, the electrochemical active surface area (ECSA), which can be affected by the two different crystal structures, was estimated via determination of the double-layer capacitance (C_{dl}) using the cyclic voltammetry (CV) method in a non-Faradaic region (Figure

S4a,b, Supporting Information). As shown in Figure S4c, Supporting Information, HES1CoCr and HES2CoCr have almost the same C_{dl} of 0.68 mF cm^{-2} and ECSA of 17 cm^2 , indicating that the difference in the microscopic crystal structure ($Pa-3$ and $Pnma$) of the nanoparticles hardly affects the ECSA and therefore the OER activity is more related to elemental composition and electronic structure when morphology is quite similar.

To further elucidate the reason for the different OER activity of the HESs, electrochemical impedance spectroscopy (EIS) measurements were performed for all HESs (Figure 4e). The semicircles in the Nyquist plots represent the charge-transfer resistance (R_{ct}) at lower frequencies. Among all HESs, HESMo shows the smallest semicircle, that is, the smallest R_{ct} and the fastest charge transfer, which also leads to and further explains the observed better OER performance. In the case of HES2 materials, HES2CoCu has the lowest R_{ct} value, which also favors and accounts for the higher OER activity. If we now compare again the previously discussed influence of the M to S ratio, the EIS results also show that HES1CoCr has a smaller semicircle than HES2CoCr, indicating a faster charge transfer during OER and thus also providing a further explanation for the better OER activity of HES1CoCr.

In the following, the durability of the two best performing materials with $Pnma$ and $Pa-3$ structure, HESMo and HES2CoCu, respectively, were investigated by chronopotentiometric measurements (Figure 4f). HESMo shows an extremely small increase in potential (7 mV) after 20 h at a constant current

of 10 mA cm^{-2} in the $E-t$ measurement. In contrast, the potential of HES2CoCu initially decreases by 17 mV until about 10 h before slightly increasing again by 4 mV until 20 h. However, the negligible changes in $E-t$ curves of HESMo and HES2CoCu indicate that both are excellent alkali-stable OER catalysts. To further investigate the rate-based stability, a multistep chronopotentiometry measurement was performed at continuous different current densities of 10, 20, and 50 mA cm^{-2} (Figure S5, Supporting Information). With the gradual increase of current density, the overpotentials of HESMo and HES2CoCu increase slightly and reach a plateau quickly, indicating good rate capability. The good rate test stability can probably be attributed to the high-entropy effect to stabilize the structure and therefore may also be a reason for the overall better OER stability.^[22]

Since the electronic structure greatly affects the catalytic properties of materials, the chemical state of the elements and elemental composition in the surface region of the best performing material HESMo was investigated by X-ray photoelectron spectroscopy (XPS), the corresponding survey spectrum is shown in Figure 5a. In brief, the spectrum indicates the presence of nickel (Ni2p), cobalt (Co2p), titanium (Ti2p), iron (Fe2p), molybdenum (Mo3d), sulfur (S2p), carbon (C1s), and oxygen (O1s). The results of detailed measurements in the S2p, Mo3d, and Ti2p region are presented in Figure 5b–d, further detail spectra (O1s, Fe2p, Co2p and Ni2p) are collected in Figure S6, Supporting Information. The detail spectrum in the S2p region (Figure 5b) is dominated by the peak doublet of metal sulfide

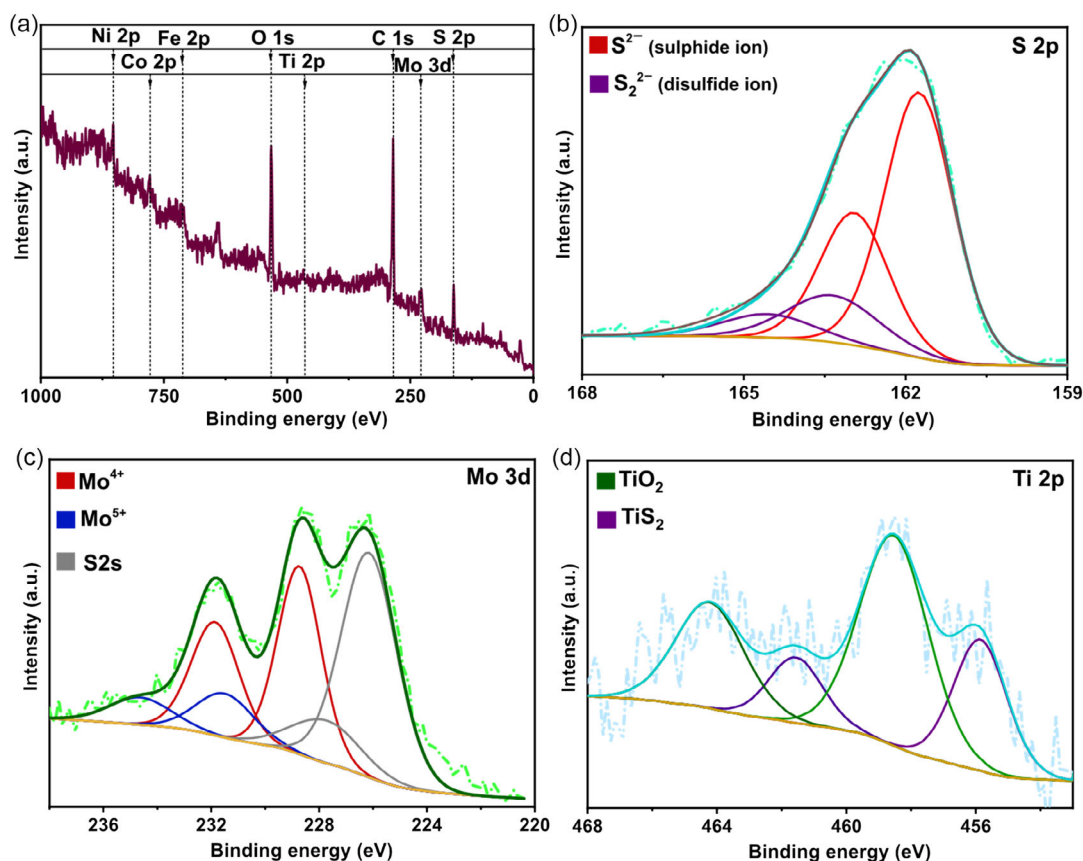


Figure 5. X-ray photoelectron spectroscopy (XPS) spectra of HESMo. a) Survey spectrum, and detail spectra in the b) S2p, c) Mo3d, and d) Ti 2p region.

species (S^{2-} , $S_{2p_{3/2}}$ at 161.8 eV). In addition, another other contribution with much smaller intensity can be observed at slightly higher binding energy, which can be attributed to disulfide ions (S_2^{2-} , $S_{2p_{3/2}}$ at 163.4 eV), commonly encountered in the case of metal sulfides.^[41]

In the Mo3d detail spectrum (Figure 5c), apart from the two S_{2s} peaks corresponding to S^{2-} and S_2^{2-} , two Mo3d peak doublets can be discerned. The first doublet ($Mo_{3d_{5/2}}$ at 228.7 eV) is due to Mo^{4+} species, both sulfide and/or oxide are possible here; the second one ($Mo_{3d_{5/2}}$ at 231.5 eV) is most probably related to Mo^{5+} species, since the $Mo_{3d_{5/2}}$ peak of Mo^{6+} should appear at even higher binding energy (232.5–233 eV).^[42,43] The detail spectrum in the Ti2p region (Figure 5d) shows two peak doublets, which can be assigned to TiS_2 ($Ti_{2p_{3/2}}$ at 455.9 eV) and TiO_2 ($Ti_{2p_{3/2}}$ at 458.5 eV), respectively. This result demonstrates the presence of some oxide species at the surface of the HESMo particles, which is also corroborated by the detection of the peak from metal oxides at 530.3 eV in the O1s spectrum (Figure S6d, Supporting Information). These species are most probably related to an interaction of the HSEMo with oxygen traces during measurement preparation and storage in the glove box.

The analysis of the other transition metals (Fe2p, Co2p, and Ni2p; Figure S6a–c, Supporting Information) is complicated by multiplet splitting effects;^[44] we therefore refrained from a peak fit and will only briefly discuss the shape and position of the spectra. For Co and Ni, the position of the main $2p_{3/2}$ peaks ($Co_{2p_{3/2}}$ at 778.9 eV, $Ni_{2p_{3/2}}$ at 853.5 eV), as well as the detection of the satellite feature at ≈ 787 eV in the case of Co, point to a preferred oxidation state +II for these two metals. The low intensity of the Fe_{2p} peak doublet and the presence of a Co and Ni Auger features overlapping with the $Fe_{2p_{3/2}}$ peak render an analysis of the results in this region impossible.

The ability of Mössbauer spectroscopy to discern even the slightest changes in the oxidation state and chemical environment of iron makes it a valuable tool for investigating the behavior of Fe in different stoichiometric ratios and crystal structures of host materials. In a previous study, Mössbauer spectroscopy was utilized to gain insights into the behavior of Fe in HESs with M_1S_1 stoichiometry and a $Pnma$ structure, as well as those with M_1S_2 stoichiometry and a $Pa-3$ structure.^[24] Specifically, the Mössbauer spectrum of HES1CoCr (as an exemplar of M_1S_1 HESs) was fitted with a single doublet, indicating that each incorporated Fe is located in a highly uniform chemical environment with an oxidation state of +II. In contrast, the Mössbauer data of HES2CoCr (as an exemplar of M_1S_2 HESs) revealed two quadrupole doublets sub-spectra, which suggested the presence of two distinct Fe environments, both with an oxidation state of +III. The majority of the Fe^{3+} species was assigned to metal sulfides, while the other Fe^{3+} species was attributed to a slightly oxidized surface. Given that the HES materials investigated in this study share similar structures and incorporated elements, it is reasonable to assume that they also feature the same oxidation states of Fe.

It is known that most transition-metal sulfides act as “pre-catalysts.” The truly catalytically active oxides/hydroxides form on the surface after self-reconstruction. This surface self-reconstruction activated by electrochemistry could help to increase the amount and activity of the surface active sites

and improve the OER performance.^[45,46] Most probably, the HESs also act as “pre-catalysts.” In addition, the tunability of the composition and electronic structure of the surface of HEMs provides a variety of possible atomic configurations on the catalyst surface due to the presence of multiple elements.^[47] According to previous reports,^[2,3,23] metal sulfides M–S and some amorphous surface sulfates react with hydroxyl radicals to form metal hydroxide M–OH and sulfate anions during OER in alkaline medium. Subsequently, more OH^- is adsorbed on M–OH to form the intermediate metal-oxide M–O and then metal-oxide hydroxide M–OOH. Then, the sulfate-containing MOOH or MOOH–S decomposes into oxygen and the free active site. During this process, cocktail effects from the synergy of multiple metals together with the strong interaction between metal and sulfur modulate the charge state and enhance the OER catalytic activity and stability.^[22,23,28] Not only for HESs but also for other high-entropy systems, such as alloys and oxides, the superiority of high-entropy catalysts has been investigated and confirmed by computationally assisted methods (e.g., density-functional theory).^[22,47–49]

The use of HESs as OER catalysts also makes it possible to minimize the concentration of noble metals in catalysts (e.g., Ir in IrO_2), enabling low-cost high-performance materials with high OER performance. The HESs presented here are also mostly free of noble metals, but still show improved catalytic activity compared to IrO_2 . **Figure 6** provides a final comparison of the catalytic activity of all materials: the higher the current density at a given overpotential, the better the catalyst performance. Seven out of ten materials show improved performance compared to the state-of-the-art OER catalyst IrO_2 . Previous studies on HESs as OER catalysts^[22,23,25] used various self-supporting substrates (e.g., Ni foams, carbon sheets, and PET films with silver paste) as working electrodes, which could also promote OER performance. To facilitate the comparison with other reported materials, all the HESs prepared in this way were measured using a common glassy carbon working electrode in a three-electrode system. The comparison of OER performance between HESMoMn and the reported transition-metal sulfides is shown in Table S2, Supporting Information. Additionally, by comparing the ten HESs samples with each other, the summary about the effects of compositions and structures on

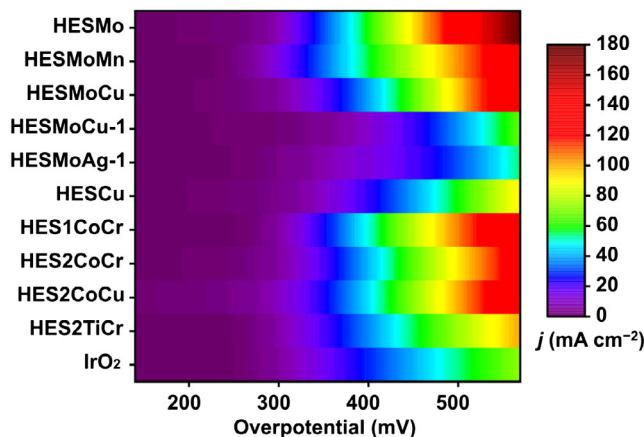


Figure 6. Comparison of current densities (j) among the HESs and IrO_2 .

OER catalytic performance is presented in Table S3, Supporting Information.

3. Conclusion

In summary, this work presents seven HESs with *Pnma* structure (M:S≈1:1) and three HESs with *Pa-3* structure (M:S = 1:2) prepared by a facile mechanochemical synthesis. The structure and morphology were studied by XRD, ICP-OES, SEM, TEM, EDX, and XPS. The HES powders with the different compositions and structures are investigated and compared as OER catalysts in a typical three-electrode setup. Most of them show promising OER performance under alkaline conditions and outperform the reference OER catalyst, IrO₂. The improvement in catalytic performance with the addition of Mo is evident. HESMo is found to exhibit superior OER activity with low overpotentials of 205, 303, and 460 mV at current densities of 1 (onset), 10, and 100 mA cm⁻², respectively. With the same metal composition but different crystal structure, the catalytic OER activity of *Pnma* HES1CoCr is compared with that of *Pa-3* HES2CoCr. HESs with both structures show promising stability in alkaline electrolytes (chronopotentiometry). The cocktail effects introduced by multiple incorporated metals and metal-sulfur interactions, as well as tailoring the electronic state of the materials, can improve the OER performance. This study reveals a new, previously unexploited class of HES that can contribute to the future development of advanced catalysts.

4. Experimental Section

Synthesis: All reagents were purchased from commercial sources (Sigma Aldrich/Alfa Aesar, Purity ≥99%) and used without further purification. HES1CoCr, HES2CoCr, HES2CoCu, and HES2TiCr were prepared by a high-energy planetary ball-milling process, more details can be found elsewhere.^[24] For the synthesis of HESMo, HESMoMn, HESMoCu, and HESCu, metal-sulfide powders (FeS, Ni₃S₂, CoS, TiS₂, MoS₂, MnS, and CuS) were ball-milled for 14 h in the respective metal ratio. Similarly, for the synthesis of HESMoCu-1 and HESMoAg-1, the corresponding metal-sulfide powders (FeS, Ni₃S₂, CoS, TiS₂, MoS₂, Cu₂S, and Ag₂S) were mixed according to the respective metal ratio. All HESs were ball-milled in a high-energy planetary ball-milling machine (Retsch PM 100, Retsch GmbH) at 500 rpm using 50 mL WC vials and 5 mm diameter WC balls under argon atmosphere. The weight ratio of balls to precursors was 40:1.

Materials Characterization: Powder XRD was carried out with powder samples at room temperature, using an STOE Stadi P diffractometer, equipped with a Ga-jet X-ray source (Ga-K_β radiation, 1.2079 Å). Refinement of the XRD pattern was performed using TOPAS Academics V5 software. Si served as a calibration sample to determine the instrumental resolution. The samples for ICP-OES were dissolved in aqua regia (HCl: HNO₃, 3:1) and analyzed by performing a double determination using an ARCOS ICP-OES (Spectro Analytical Instruments, Kleve, Germany) with axial plasma view. SEM measurements were performed on powder samples using a ZEISS Gemini Leo 1530. TEM measurements, including SAED, HR-TEM, and STEM-EDX, were done on a ThermoScientific Themis 300 microscope, equipped with a HAADF-STEM detector and Super-X EDX detector. The microscope was operated at an accelerating voltage of 300 kV. The powder samples were dispersed on a holey carbon-coated gold grid and loaded onto a FEI double-tilt holder. XPS measurements were carried out with a Phoibos 150 spectrometer system (Specs) using monochromatized Al K_α radiation (400 W, 15 kV), a detection angle of 45°, and pass energies at the analyzer of 90 and 30 eV for survey and detail measurements, respectively. The C 1s peak of adventitious carbon at 284.8 eV was

used as reference for binding energy calibration. Peak fitting of the measurement results was done with CasaXPS software, using Gaussian–Lorentzian peak shapes and the expected values for intensity ratios and spin–orbit splitting of the various peak doublets.^[50] The contribution of S2s peaks from the various S species in the Mo3d detail spectrum was accounted by entering corresponding peaks. The positions of these S2s peaks were fixed by assuming a constant distance between S2p and S2s peak of 64.4 eV (known from previous work with MoS₂), the intensities were related to the S2p peaks by considering the relative sensitivity factors of the S2p and S2s peaks.

Electrochemistry: Electrochemical measurements were conducted using a three-electrode setup on a modulated speed rotator (Equilibrium SAS) with a rotating glassy carbon working electrode (*A* = 0.196 cm²), a Pt spiral serving as the counter electrode, and Ag/AgCl serving as the reference electrode. The working electrode was prepared by mixing 10 mg of the active material in a solution consisting of 1800 μL of 2-propanol, 100 μL of H₂O, and 100 μL of Nafion (5 wt% Nafion in water/1-propanol, VWR). The mixture was sonicated in an ultrasonic finger/homogenizer (Scientz-11D, Scientz) in an ice water bath for 30 min. Subsequently, 8 μL of the solution (aliquot) was dropped onto the surface of the working electrode and dried, resulting in a catalyst loading of 0.20 mg cm⁻². As reference material, iridium oxide powder was used (IrO₂, 99 % Alfa Aesar). The electrocatalytic OER measurements were performed in an O₂-saturated electrolyte of 1 M KOH (90 %, reagent grade, Sigma Aldrich) at room temperature using a potentiostat (BioLogic GmbH). All measurements were done at rotation speeds of 1600 rpm. LSV was performed at a sweep rate of 5 mV s⁻¹ in a potential range from 1.0 to 1.8 V versus reversible hydrogen electrode (RHE). The Tafel slope was derived from LSV. The measured potentials are referred to the RHE, $E_{\text{RHE}} = E_{\text{Ag/AgCl}} + 0.059 \text{ pH} + E^{\theta}_{\text{Ag/AgCl vs RHE}}$, where $E^{\theta}_{\text{Ag/AgCl vs RHE}}$ is 0.1976 at 25 °C and the pH of the electrolyte was measured by pH meter as 13.3. The overpotential $\eta = E_{\text{RHE}} - 1.23 \text{ V}$. No iR correction was applied. The electrochemical *C_{dl}* was evaluated via CV measurement in a non-Faradaic potential range (0.877 – 0.977 V vs. RHE) using five different scan rates (5, 10, 20, 40, and 60 mV s⁻¹). The ECSA was calculated according to the equation $\text{ECSA} = C_{\text{dl}}/C_s$, with a specific capacitance, *C_s* of 0.04 mF cm⁻² according to literature.^[22,51] EIS measurements were performed at an overpotential of 400 mV in a frequency range from 1 to 100 kHz with an AC amplitude of 10 mV. The durability properties of HESs were compared by chronopotential E–t curves at current densities of 10, 20, and 50 mA cm⁻².

Supporting Information

Supporting Information is available from the Wiley Online Library or from the author.

Acknowledgements

L.L. acknowledges financial support from the China Scholarship Council (CSC). S.S. and B.B. acknowledge the support from EPISTORE and enABLES, projects funded by the European Union's Horizon 2020 research and innovation program under grant agreement nos. 101017709 and 730957, respectively. Z.D. acknowledge the Karlsruhe Nano Micro Facility at Karlsruhe Institute of Technology for providing TEM access. G.K. and M.F. gratefully acknowledge financial support by Deutsche Forschungsgemeinschaft (DFG, German Research Foundation) under Germany's Excellence Strategy, EXC 2154, project number 390874152. Financial support by Deutsche Forschungsgemeinschaft is acknowledged by HH (HA 1344/45-1) and (HA 1344/43-2).

Open Access funding enabled and organized by Projekt DEAL.

Conflict of Interest

The authors declare no conflict of interest.

Data Availability Statement

The data that support the findings of this study are available from the corresponding author upon reasonable request.

Keywords

catalysts, high-entropy materials, high-entropy sulfides, oxygen evolution reaction

Received: February 14, 2023

Revised: April 27, 2023

Published online:

- [1] J. O. Bockris, *J. Chem. Phys.* **1956**, *24*, 817.
- [2] A. Badruzzaman, A. Yuda, A. Ashok, A. Kumar, *Inorg. Chim. Acta* **2020**, *511*, 119854.
- [3] N. T. Suen, S. F. Hung, Q. Quan, N. Zhang, Y. J. Xu, H. M. Chen, *Chem. Soc. Rev.* **2017**, *46*, 337.
- [4] Y. Sun, T. Zhang, C. Li, K. Xu, Y. Li, *J. Mater. Chem. A* **2020**, *8*, 13415.
- [5] S. R. Ede, Z. Luo, *J. Mater. Chem. A* **2021**, *9*, 20131.
- [6] S. Anantharaj, S. R. Ede, K. Sakthikumar, K. Karthick, S. Mishra, S. Kundu, *ACS Catal.* **2016**, *6*, 8069.
- [7] Q. Wang, L. Velasco, B. Breitung, V. Presser, *Adv. Energy Mater.* **2021**, *11*, 2102355.
- [8] C. M. Rost, E. Sacht, T. Borman, A. Moballegh, E. C. Dickey, D. Hou, J. L. Jones, S. Curtarolo, J. P. Maria, *Nat. Commun.* **2015**, *6*, article no. 8485.
- [9] A. Sarkar, L. Velasco, D. Wang, Q. Wang, G. Talasila, L. de Biasi, C. Kuebel, T. Brezesinski, S. S. Bhattacharya, H. Hahn, B. Breitung, *Nat. Commun.* **2018**, *9*, 3400.
- [10] E. P. George, D. Raabe, R. O. Ritchie, *Nat. Rev. Mater.* **2019**, *4*, 515.
- [11] J. Yeh, S. Chen, S. Lin, J. Gan, T. Chin, T. Shun, C. Tsau, S. Chang, *Adv. Eng. Mater.* **2004**, *6*, 299.
- [12] N. J. Usharani, P. Arivazhagan, T. Thomas, S. S. Bhattacharya, *Mater. Sci. Eng., B* **2022**, *283*, 115847.
- [13] N. Sreenivasulu, U. N. Kumar, K. M. V. V. Madhav, T. Thomas, S. S. Bhattacharya, *ChemistrySelect* **2022**, *7*, 202104015.
- [14] T. Jin, X. Sang, R. R. Unocic, R. T. Kinch, X. Liu, J. Hu, H. Liu, S. Dai, *Adv. Mater.* **2018**, *30*, 1707512.
- [15] P. Sarker, T. Harrington, C. Toher, C. Oses, M. Samiee, J. P. Maria, D. W. Brenner, K. S. Vecchio, S. Curtarolo, *Nat. Commun.* **2018**, *9*, 4980.
- [16] X. Yan, L. Constantin, Y. Lu, J. Silvain, M. Nastasi, B. Cui, *J. Am. Ceram. Soc.* **2018**, *101*, 4486.
- [17] P. A. Sukkurji, Y. Cui, S. Lee, K. Wang, R. Azmi, A. Sarkar, S. Indris, S. S. Bhattacharya, R. Kruk, H. Hahn, Q. Wang, M. Botros, B. Breitung, *J. Mater. Chem. A* **2021**, *9*, 8998.
- [18] T. Wang, H. Chen, Z. Yang, J. Liang, S. Dai, *J. Am. Chem. Soc.* **2020**, *142*, 4550.
- [19] Y. Qin, J. X. Liu, F. Li, X. Wei, H. Wu, G. J. Zhang, *J. Adv. Ceram.* **2019**, *8*, 148.
- [20] Z. Deng, A. Olvera, J. Casamento, J. S. Lopez, L. Williams, R. Lu, G. Shi, P. F. P. Poudeu, E. Kioupakis, *Chem. Mater.* **2020**, *32*, 6070.
- [21] C. R. McCormick, R. E. Schaak, *J. Am. Chem. Soc.* **2021**, *143*, 1017.
- [22] M. Cui, C. Yang, B. Li, Q. Dong, M. Wu, S. Hwang, H. Xie, X. Wang, G. Wang, L. Hu, *Adv. Energy Mater.* **2021**, *11*, 2002887.
- [23] T. X. Nguyen, Y. Su, C. Lin, J. Ting, *Adv. Funct. Mater.* **2021**, *31*, 2106229.
- [24] L. Lin, K. Wang, A. Sarkar, C. Njel, G. Karkera, Q. Wang, R. Azmi, M. Fichtner, H. Hahn, S. Schweidler, B. Breitung, *Adv. Energy Mater.* **2022**, *12*, 2103090.
- [25] Y. Lei, L. Zhang, W. Xu, C. Xiong, W. Chen, X. Xiang, B. Zhang, H. Shang, *Nano Res.* **2022**, *15*, 6054.
- [26] H. Li, H. Zhu, S. Zhang, N. Zhang, M. Du, Y. Chai, *Small Struct.* **2020**, *1*, 2000033.
- [27] C. Oses, C. Toher, S. Curtarolo, *Nat. Rev. Mater.* **2020**, *5*, 295.
- [28] Y. Sun, S. Dai, *Sci. Adv.* **2021**, *7*, 20.
- [29] J. Zhao, J. Zhang, Z. Li, X. Bu, *Small* **2020**, *16*, 2003916.
- [30] D. Li, H. Liu, L. Feng, *Energy Fuels* **2020**, *34*, 13491.
- [31] Y. Xu, A. Sumbuja, A. Groves, T. Ashton, Y. Zong, J. A. Darr, *RSC Adv.* **2020**, *10*, 41871.
- [32] T. Bao, Y. Xia, J. Lu, C. Zhang, J. Wang, L. Yuan, Y. Zhang, C. Liu, C. Yu, *Small* **2022**, *18*, 2103106.
- [33] F. Dong, Y. Meng, W. Han, H. Zhao, Z. Tang, *Sci. Rep.* **2019**, *9*, article no. 12056.
- [34] L. Li, G. Li, Y. Zhang, W. Ouyang, H. Zhang, F. Dong, X. Gao, Z. Lin, *J. Mater. Chem. A* **2020**, *8*, 25687.
- [35] T. Tang, W. J. Jiang, S. Niu, N. Liu, H. Luo, Y. Y. Chen, S. F. Jin, F. Gao, L. J. Wan, J. S. Hu, *J. Am. Chem. Soc.* **2017**, *139*, 8320.
- [36] O. Diaz-Morales, I. Ledezma-Yanez, M. T. M. Koper, F. Calle-Vallejo, *ACS Catal.* **2015**, *5*, 5380.
- [37] Y. Mei, Y. Feng, C. Zhang, Y. Zhang, Q. Qi, J. Hu, *ACS Catal.* **2022**, *12*, 10808.
- [38] Y. Deng, A. D. Handoko, Y. Du, S. Xi, B. S. Yeo, *ACS Catal.* **2016**, *6*, 2473.
- [39] L. Gong, J. Koh, B. S. Yeo, *ChemSusChem* **2018**, *11*, 3790.
- [40] M. S. Burke, M. G. Kast, L. Trotochaud, A. M. Smith, S. W. Boettcher, *J. Am. Chem. Soc.* **2015**, *137*, 3638.
- [41] V. Fominiski, M. Demin, V. Nevolin, D. Fominiski, R. Romanov, M. Gritskovich, N. Smirnov, *Nanomaterials* **2020**, *10*, 653.
- [42] G. Tai, T. Zeng, J. Yu, J. Zhou, Y. You, X. Wang, H. Wu, X. Sun, T. Hu, W. Guo, *Nanoscale* **2016**, *8*, 2234.
- [43] J. G. Choi, L. T. Thompson, *Appl. Surf. Sci.* **1996**, *93*, 143.
- [44] M. C. Biesinger, B. P. Payne, A. P. Grosvenor, L. W. M. Lau, A. R. Gerson, R. S. C. Smart, *Appl. Surf. Sci.* **2011**, *257*, 2717.
- [45] S. Jin, *ACS Energy Lett.* **2017**, *2*, 1937.
- [46] W. Wang, S. Zhu, X. Chen, X. Zhang, Y. Tao, Y. Zhang, R. Xiang, X. Wu, *Nanotechnology* **2020**, *31*, 475402.
- [47] T. X. Nguyen, Y. C. Liao, C. C. Lin, Y. H. Su, J. M. Ting, *Adv. Funct. Mater.* **2021**, *31*, 2101632.
- [48] H. Liu, L. Syama, L. Zhang, C. Lee, C. Liu, Z. Dai, Q. Yan, *SusMat* **2021**, *1*, 482.
- [49] L. Sharma, N. Kumar Katiyar, A. Parui, R. Das, R. Kumar, C. Sekhar Tiwary, A. K. Singh, A. Halder, K. Biswas, *Nano Res.* **2022**, *15*, 4799.
- [50] J. F. Moulder, J. Chastain, in *Handbook of X-Ray Photoelectron Spectroscopy: A Reference Book of Standard Spectra for Identification and Interpretation of XPS Data*, Eden Prairie, Physical Electronics Division, Perkin-Elmer Corp., Minn, MA **1992**.
- [51] C. C. L. McCrory, S. Jung, J. C. Peters, T. F. Jaramillo, *J. Am. Chem. Soc.* **2013**, *135*, 16977.